Digest Journal of Nanomaterials and Biostructures

Dig. J. Nanomater. Bios. **2026**; 21(2): 54282
https://doi.org/10.31083/DJNB54282

Original Research

Enhancing the Tribological Properties of 12Cr2Ni4A Steel Through Nanodiamond Thermal Diffusion: A Molecular Simulation Study

Lei Wei[1,2], Yixuan Li[1], Pan Xie[1], Yuelin Chen[1], Haoye Wang[1], Minghui Xiong[1], Chao Li[1], Xiaohong Zhang[1], Song Chen[1,*]

[1]Laboratory of Intelligent Manufacturing and Service Performance Optimization of Laser and Grinding in Mechanical Industry, School of Mechanical Engineering, Hunan Institute of Science and Technology, 414006 Yueyang, Hunan, China
[2]State Key Laboratory of Special Materials Surface Protection, China Academy of Machinery Wuhan Research Institute of Materials Protection Co., Ltd., 430030 Wuhan, Hubei, China
*Correspondence: chensong@hnist.edu.cn (Song Chen)
Academic Editors: Maria Harja and Carmen-Georgeta Ristoscu
Submitted: 27 November 2025 Revised: 2 February 2026 Accepted: 5 March 2026 Published: 27 May 2026

Abstract

12Cr2Ni4A steel is widely used in rail transportation and the aerospace industry as a component of gears and shafts. The continuous increase in the power density of mechanical equipment necessitates the development of methods for enhancing the tribological properties of 12Cr2Ni4A steel. Herein, we achieved this goal using the thermal diffusion of nanodiamond (carbon source) in 12Cr2Ni4A steel and analyzed the effects of diffusion temperature on steel microhardness, tribological properties, and microstructural characteristics. A microstructural model of nanodiamond and 12Cr2Ni4A steel was constructed using molecular dynamics methods to analyze the structural evolution patterns of nanodiamond and the matrix material during thermal diffusion. Compared with untreated 12Cr2Ni4A steel, the best-performing sample exhibited a 110.68% higher hardness, 59.81% lower wear mass loss, and 41.35% lower average coefficient of friction. Molecular dynamics simulations indicated that nanodiamond enters Fe, Cr, and Ni lattices as free C atoms, ultimately forming abundant Fe–C, Cr–C, and Ni–C bonds with FeCrNi crystals and thus markedly improving the compactness and bonding strength of the diffusion layer and enhancing its tribological properties. This work provides a new strategy for enhancing the tribological properties of 12Cr2Ni4A steel, deepens the understanding of the mechanism of nanodiamond incorporation–induced reinforcement at the atomic scale, and provides valuable theoretical insights.

Keywords: nanodiamond; 12Cr2Ni4A steel; thermal diffusion; friction and wear

1. Introduction

12Cr2Ni4A steel is an alloy structural steel with high strength, high toughness and good hardenability, mainly used for manufacturing key mechanical components such as gears, shafts that bear high loads and alternating stress. Its excellent mechanical properties have enabled it to be widely applied in multiple high-end industrial fields. While, mechanical equipment is now moving towards high speed, heavy load, and high temperature [1–4]. 12Cr2Ni4A components impose higher requirements on tribological properties. Traditional methods to enhance the tribological properties of 12Cr2Ni4A steel include ion implantation, laser strengthening, and ultrasonic vibration grinding [5].

Scholars conducted extensive research on ion implantation of 12Cr2Ni4A steel to enhance the surface properties of 12Cr2Ni4A alloy steel. Dong *et al.* [5] employed Ti+N dual-element implantation technology for surface modification. The microstructure, mechanical properties, and corrosion behavior of the modified layer were investigated. Results showed that the nano-hardness and corrosion resistance of the Ti+N co-implanted layer were significantly superior to those of the untreated samples. It indicated that the formation of nano-ceramic phases and structures is not the sole factor affecting the nano-hardness and corrosion resistance of the material, and there may be deeper strengthening mechanisms. Dong *et al.* [6] used lanthanum and cerium ion implantation to assist low-pressure vacuum carburizing of 12Cr2Ni4A steel. The results revealed that lanthanum and cerium implantation could improve the microstructure of the vacuum carburized layer and enhance the uniformity of carbon element distribution on the carburized surface. Meanwhile, rare earth implantation played a positive role in increasing surface hardness and carburizing rate. Lanthanum showed a more significant effect on surface hardness and retained austenite content than cerium. However, despite the ability of ion implantation technology to improve the surface hardness and wear resistance of 12Cr2Ni4A steel to a certain extent, it still suffers from limitations such as limited depth of the modified layer, the need for additional heat treatment steps to repair lattice damage, and complex processes, which severely affect its service life and application potential.

There are studies used laser shock processing to strengthen 12Cr2Ni4A steel. Wang *et al.* [7] designed different welding experiments to verify the effect of laser shock strengthening on 12Cr2Ni4A material, using preci-

sion micro-beam plasma arc welding and gas metal arc welding in the welding tests. The results showed that laser shock processing could effectively eliminate welding residual tensile stress and improve the fatigue performance and service life of welded joints. Zhao *et al*. [8] proposed a rectangular laser heat source model to improve laser quenching efficiency and achieve precise process control. This model was constructed based on the characteristics of actual laser processing heat sources. A numerical model coupling temperature, stress, and phase transformation was developed for double lap laser quenching of 12Cr2Ni4A aircraft gears, unveiling the transient evolution of the process. Numerical simulation results revealed the temperature characteristics of rapid heating and cooling during laser quenching, and a residual stress concentration distribution was observed in the secondary tempering zone. Phase transformation analysis post-quenching indicated a significant presence of martensite in the quenched layer. Finally, the validity of the numerical simulation was verified through laser quenching experiments on aircraft gears. However, although laser treatment can prepare a hardened layer with excellent performance on the surface of 12Cr2Ni4A steel, it has disadvantages such as high equipment cost, strict process parameter requirements, and limited processing depth, which severely affect its popularization and application in some fields.

Researchers conducted ultrasonic vibration grinding to enhance 12Cr2Ni4A steel. Wen *et al*. [9] examined the formation mechanism of residual stress during ultrasonic vibration grinding of high-strength alloy steel, as well as the correlation between processing parameters and residual stress. Through kinematic analysis, they derived formulas for ultrasonic grinding force and the temperature field of transient moving heat sources, developed a thermo-mechanical coupling residual stress prediction model via the finite element method and validated it with experiments. Integrated with thermal behavior analysis, they elucidated the formation mechanism of residual stress and ultimately obtained comprehensive process parameter rules through simulation and experiments. The results demonstrated that compared with conventional grinding (CG), ultrasonic vibration grinding can reduce grinding temperature by approximately 8%. Ultrasonic vibration grinding maintains a larger residual compressive stress, effectively inhibiting the occurrence of tensile stress. Lei *et al*. [10] constructed a mathematical model for the surface residual stress of hardened 12Cr2Ni4A alloy steel during ultrasonic vibration-assisted online electrolytic dressing grinding. They explored the stress state of the machined surface under different grinding methods, assessed the influence of diverse parameters in Ultrasonic Vibration-Assisted ELID Grinding (UVAEG) on the workpiece surface residual stress, and validated their findings experimentally. The results indicated that the effects of grinding depth, ultrasonic amplitude, and duty cycle on the workpiece surface residual stress were generally consistent with the established residual stress model, validating the model's reliability. Collectively, the ion implantation method exhibits a shallow implantation layer. Laser strengthening faces challenges in process control, poor geometric adaptability, and insufficient cost-effectiveness [11–13]. Ultrasonic vibration grinding is constrained by limitations such as limited processing efficiency and a high technical threshold. These shortcomings impede meeting mass production requirements.

Nanoparticles are also used to enhance the tribology performance of materials [14]. Among various nanoparticles, nano-diamond has attracted significant attention due to its unique combination of properties [15–17]. Compared to other carbon materials such as carbon nanotubes and graphene, nano-diamond not only possesses extremely high hardness, excellent chemical stability, and superior thermal conductivity but also exhibits outstanding interfacial compatibility with different matrix materials [18,19]. It has been widely used to reinforce polymer, ceramic, and metal matrix composites, demonstrating great potential in fields such as aerospace, biomedicine, and precision machinery [20,21].

12Cr2Ni4A steel was taken as the research subject. Nano-diamond was taken as a carbon source to infiltrate 12Cr2Ni4A steel with thermal diffusion, aimed to improve its surface microstructure and tribological properties. The aim is to elucidate the functional mechanism of nano-diamond during the thermal diffusion process of 12Cr2Ni4A steel, focusing on analyzing its influence on the material's microstructural evolution, interface bonding characteristics, and friction-wear behavior. By revealing the multi-scale strengthening mechanism induced by nano-diamond, the study seeks to enhance the service reliability of 12Cr2Ni4A steel under heavy load and complex working conditions.

This work provides a new technical approach for the surface strengthening design of high-performance mechanical structural components. The mechanism of the nano-diamond particles to enhance 12Cr2Ni4A steel was revealed which can give theoretical guides for wide application.

2. Experimental Details

2.1 Thermal Diffusion Experiment of 12Cr2Ni4A Steel

The nano-diamond powder used in this work was purchased from Henan Zhenzuan Abrasive Tools Co., Ltd. (Zhengzhou, Henan, China). The information on particles was shown in Tables 1,2.

Considering the comprehensive balance of cost and quality, this study adopts nano-diamond particle material with an average particle size of 30 nm for thermal diffusion experiments. Its surface morphology was observed using a scanning electron microscope (SEM) ZEISS Sigma300 SEM (Oberkochen, Germany) as shown in Fig. 1.

Table 1. Particle size range of nano-diamond powder.

Diam.Range (μm)	0.0101–0.0171	0.0171–0.0289	0.0289–0.0487	0.0487–0.0822	0.0822–0.1387	0.1387–0.2341
Fraction (%)	33.45	49.75	15.01	1.18	0.51	0.10

Table 2. Weight, specific surface area and quantity parameters of nano-diamond powder.

	Mean (μm)	Median (μm)	CV%
Weight	0.0222	0.0201	49.412
Surface	0.0193	0.0176	38.750
Number	0.0158	0.0144	30.424

CV, coefficient of variation.

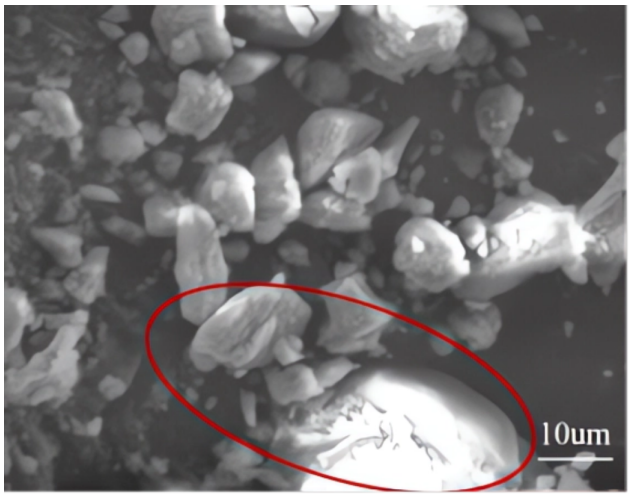

Fig. 1. Microscopic morphology diagram of nano-diamond. The red circle shows micron-scale hard agglomerates and detonation-derived unrefined particles in nanodiamond powder. This inherent high-surface-energy effect explains why the weight-based CV% in Table 2 is markedly higher than the number-based value. Scale bar = 10 μm

12Cr2Ni4A samples with dimensions of 20 mm × 10 mm × 10 mm were used. The sample surfaces were finely ground by using 600-grit SiC sandpaper (Shanghai Grinding Wheel Factory Co., Ltd., Shanghai, China), aiming to control the surface roughness within the range of 0.3–0.5 μm. Subsequently, ultrasonic cleaning was performed on the samples to remove ethanol residues. After confirming that the treated sample surfaces were flat and clean, nano-diamond powder with an average particle size of 30 nm was uniformly coated onto the surface of the prepared 12Cr2Ni4A steel samples using a clean spatula. By precisely controlling the powder amount and spreading technique, a continuous and uniform pre-deposited powder layer was formed on the surface to be treated. This method ensured maximum intimate contact between the nano-diamond and the metal substrate before the initiation of thermal diffusion, laying the foundation for the subsequent high-temperature diffusion process.

Thermal diffusion was conducted in a tubular furnace (Shenyang Kejing Auto-instrument Co., Ltd., Shenyang, Liaoning, China). During the thermal diffusion process, the system pressure was strictly controlled within 0–10 MPa. Under an argon atmosphere, the temperature was increased at a constant rate of 10 °C/min to a preset temperature range (950 °C to 990 °C, with 10 °C intervals), and held at this temperature for 4 hours.

After thermal diffusion, the samples were subjected to a 90-minute holding treatment at 850 °C, followed by rapid cooling using special quenching oil. Finally, the samples were tempered for 2 hours and then air-cooled (Fig. 2).

2.2 Hardness and Tribological Properties Test

The material hardness performance test was carried out using an HV-1000A Vickers optical microhardness tester (Zhengzhou Huayin Instrument Co., Ltd., Zhengzhou, Henan, China), as shown in Fig. 3a. A square pyramid diamond indenter was employed: A standard load of 9.8N was applied to the 12Cr2Ni4A steel sample surface, and the load was maintained for 10 seconds. The hardness value was calculated based on the average pressure per unit surface area of the square pyramid indentation. A ten-point measurement method was applied for multi-point testing, and the arithmetic mean of hardness values was calculated to yield reliable test data.

To determine the phase composition of 12Cr2Ni4A steel post-thermal diffusion, an X-ray diffraction (XRD) analysis was performed on the cross-section of the thermally diffused sample by using a DX-2700A X-ray diffractometer (Dandong Haoyuan Instrument Co., Ltd., Dandong, Liaoning, China), as shown in Fig. 3b.

A VHX-5000 super-depth-of-field 3D digital microscope, as shown in Fig. 3c (VXH-500, Keyence (Japan) Co., Ltd., Osaka, Japan), was employed for observing and analyzing the surface morphology of the 12Cr2Ni3A steel disk sample post-pin-on-disk test. The influence of different thermal diffusion treatment temperatures on the friction and wear behavior of 12Cr2Ni4A steel pin samples was investigated.

A pin-on-disk rotational friction and wear test was conducted by using an MMW-1A vertical universal friction and wear tester (Jinan Jingcheng Testing Technology Co., Ltd., Jinan, Shandong, China). The pin sample was taken as the test specimen, while the disk sample was 12Cr2Ni3A steel (55 mm in diameter). Prior to the experiment, the pin sample was weighed using a PR series balance (OHAUS Instruments (Shanghai) Co., Ltd., Shanghai, China). The test was conducted at room temperature with Mobil 600 XP 100 lubricant (ExxonMobil (Tianjin) Co., Ltd., Tian-

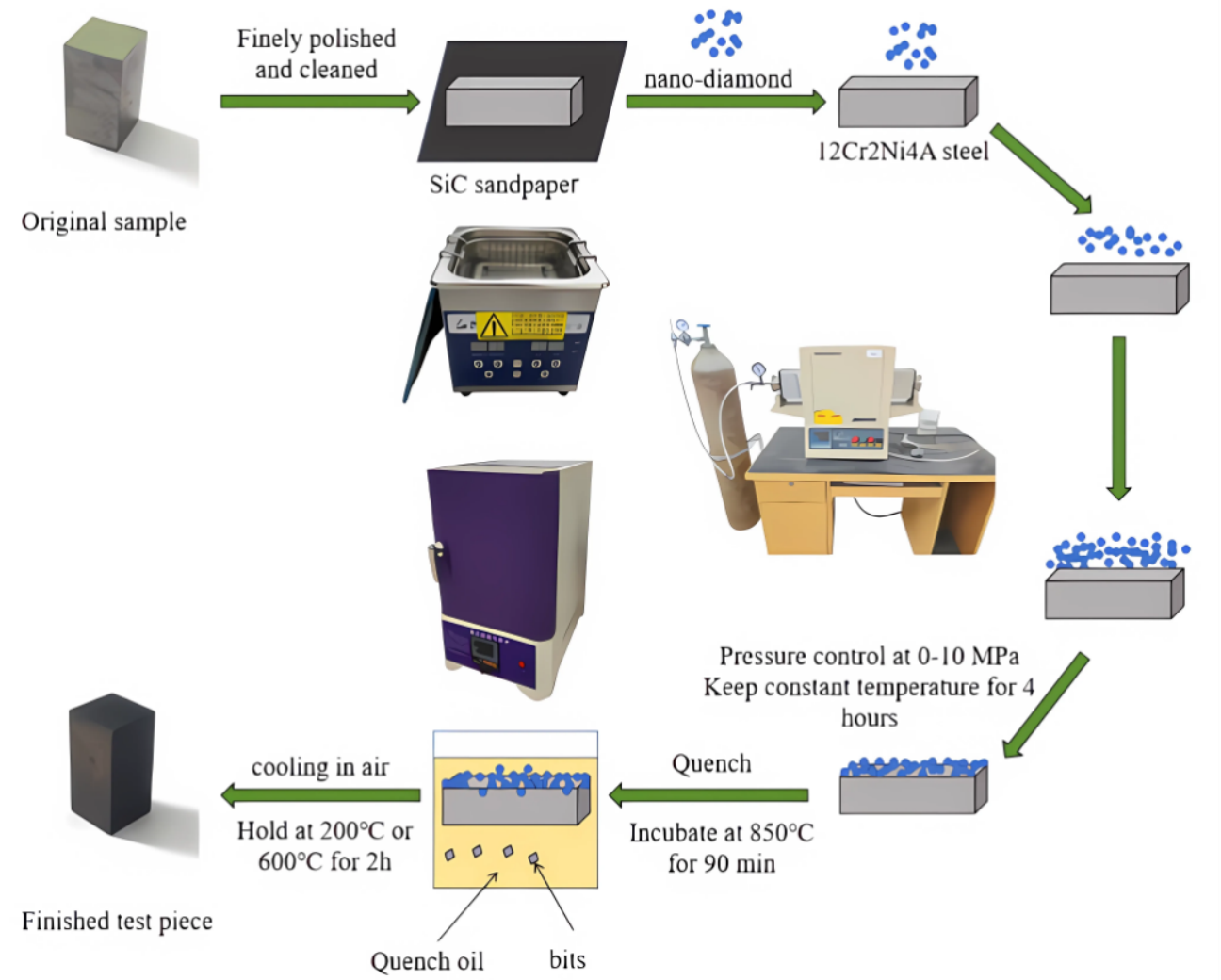

Fig. 2. Schematic diagram of the fabrication process.

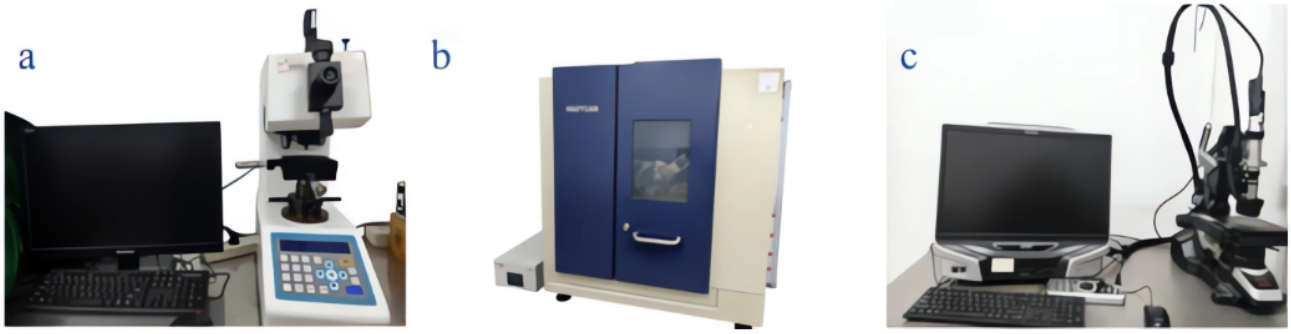

Fig. 3. Experimental instruments. (a) Huayin HV-1000A Vickers Optical Microhardness Tester. (b) DX-2700A X-ray Diffractometer. (c) Keyence VHX-5000 Super Depth of Field 3D Digital Microscope.

jin, China), 50 N normal load, 300 r/min rotational speed, and 60 min experimental time. The pin sample was cleaned and reweighed to calculate wear loss as illustrated in the schematic diagram of the friction and wear test in Fig. 4.

2.3 Molecular Dynamics Simulation

A molecular dynamics simulation method was employed to simulate the thermal diffusion process of nano-diamonds in 12Cr2Ni4A alloy. The microstructural evolution patterns of nano-diamonds and 12Cr2Ni4A were

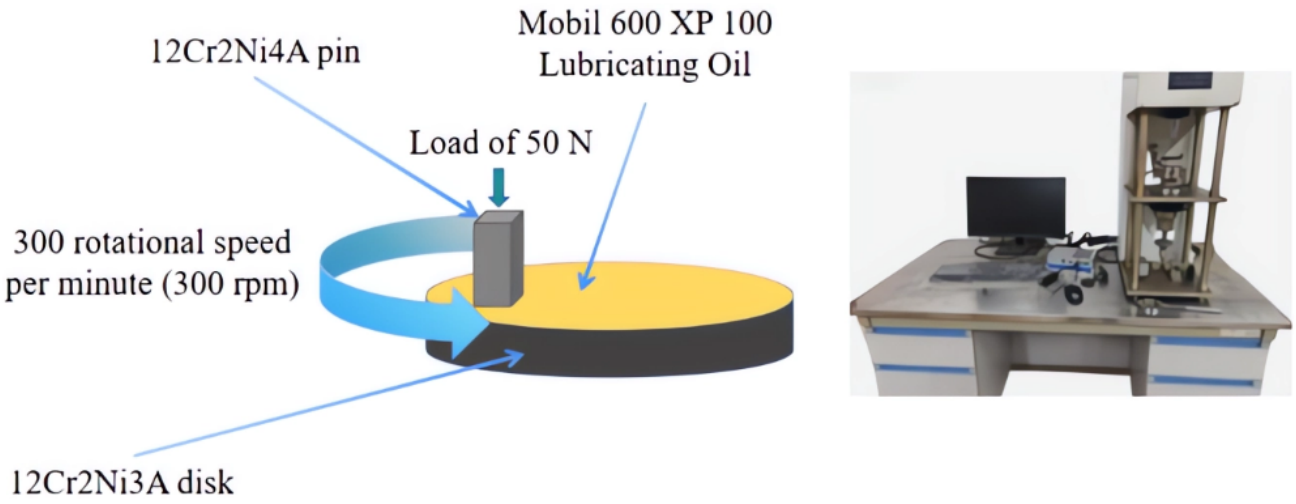

Fig. 4. Schematic diagram of friction and wear test.

analyzed. The thermal diffusion mechanism of nano-diamonds was revealed. The main elemental composition of 12Cr2Ni4A alloy was Fe, Cr, and Ni atoms. The FeCrNi alloy model structure was used to represent the 12Cr2Ni4A alloy in the molecular dynamics thermal diffusion simulation, with the model structure shown in Fig. 5. The dimensions of the simulation box along the X[1 0 0], Y[0 1 0], and Z[0 0 1] directions were 115 Å, 45 Å, and 75 Å, respectively, with slight adjustments made to satisfy periodic boundary conditions. The FeCrNi alloy model measured 115 Å, 45 Å, and 57 Å along the X, Y, and Z directions, adopting a face-centered cubic (FCC) structure (a = 3.56). The nano-diamond model had a thickness of 12 Å, and the total number of atoms in the model was 56,362. The bottom section (0–15 Å) of the alloy model was designated as a rigid body to maintain substrate stability, while the remaining section (15–75 Å) followed Newton's second law to simulate the thermal diffusion motion of nano-diamonds. To avoid non-physical interactions between the nano-diamonds and the alloy model in the initial stage, the initial position of the nano-diamonds was set 0.5 nm above the surface of the FeCrNi alloy, ensuring the accuracy and reliability of the simulation results.

Two types of potential functions were used to describe the interactions between different atoms, the Embedded Atom Method (EAM) and the Lennard-Jones (L-J) potential function. The EAM potential [22–24] is used to characterize the interactions between Fe, Cr, and Ni atoms, with its formula shown in Eqn. 1.

$$E_{ij} = F_a\left[\sum_{i\neq j}\rho_\beta\left(r_{ij}\right)\right] + \frac{1}{2}\sum_{i\neq j}\varphi_{\alpha\beta}\left(r_{ij}\right) \quad (1)$$

Where α and β denote the element types of atoms i and j, rij is the interatomic distance, $\varphi\alpha\beta$ represents the two-body potential (also referred to as the pair potential), Fα is the many-body potential, and $\rho\beta$ is the electron density contributed by atom j to atom i.

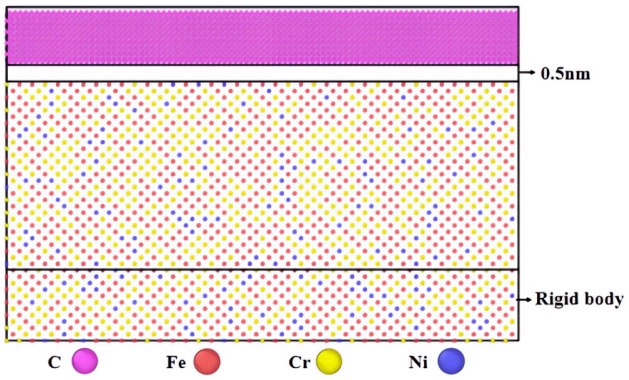

Fig. 5. Thermal diffusion model of nano-diamond particles and FeCrNi alloy.

The Lennard-Jones (L-J) potential [25,26] is used to describe the non-bonded interactions between nano-diamonds and Fe, Cr, Ni atoms [27,28], respectively. LAMMPS (LAMMPS 64-bit 19Nov2024-MSMPI) (Large-scale Atomic/Molecular Massively Parallel Simulator) includes the L-J potential and its various derived versions. The version adopted in this work is the "pair lj/cut" potential, which truncates the L-J potential at a distance rc. Its formula is shown in Eqn. 2.

$$E_{IJ} = 4\varepsilon_{ij}\left[\left(\frac{\sigma_{ij}}{r_{ij}}\right)^{12} - \left(\frac{\sigma_{ij}}{r_{ij}}\right)^{6}\right] (r < r_c) \quad (2)$$

Where εij is the minimum energy, σij is the distance at minimum energy (also known as the zero-crossing distance), and rc is the cutoff radius. The parameters of the L-J potential function used in this work are shown in Table 3.

Table 3. Parameters of L-J potential function between Fe, Cr and Ni atoms and C atoms.

Element type	ε/eV	σ/Å
Fe-C	0.5263	2.321
Cr-C	0.6732	2.281
Ni-C	0.5196	2.2395

This study investigated the thermal diffusion behavior of the nano-diamond/FeCrNi alloy system. For simulation parameter configuration—aimed at balancing calculation reliability and computational efficiency—the system was configured under the number-volume-energy (NVE) microcanonical ensemble with a 0.001 ps time step. Atomic initial velocities were assigned according to the Maxwell-Boltzmann distribution to accurately capture the system's thermodynamic properties. To maintain isothermal conditions during simulation, the Rescale temperature control algorithm was adopted. The simulation temperature protocol was strictly aligned with thermal diffusion experimental conditions: starting from an initial temperature of 293K, the system was heated to 1243K at a constant rate of 10 K/s, followed by isothermal simulation at this target temperature. To acquire detailed kinetic data, molecular dynamics trajectory information was recorded every 0.1 picoseconds.

3. Results

3.1 Analysis of Surface Microstructure and Surface Morphology

3.1.1 Analysis of Microhardness Results of 12Cr2Ni4A Steel After Thermal Diffusion

The influence of nano-diamonds on the hardness of 12Cr2Ni4A steel under varying thermal diffusion temperature conditions was shown in Fig. 6. The hardness indenter morphology image was illustrated in Fig. 7.

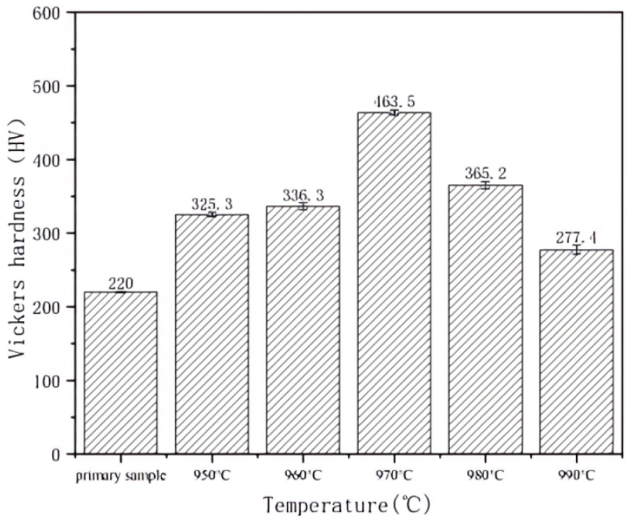

Fig. 6. Hardness of 12Cr2Ni4A gear steel at different thermal diffusion temperatures.

According to Figs. 6,7, nano-diamond thermal diffusion significantly enhanced the surface hardness of 12Cr2Ni4A steel. Within the 950–960 ℃ temperature range, the hardness manifested a notable upward trend as thermal diffusion temperature increased. When the treatment temperature rose to 970 ℃, the sample showed the superior strengthening effect following 4 hours of thermal diffusion, with surface hardness increased by 110.68% compared to the untreated sample, attaining the maximum value of all experiments. Under the 990 ℃ high-temperature condition, sample hardness increased by 26.09%, which was the least strengthening effect among all nano-diamond treated groups. The experimental data fully demonstrated a nonlinear relationship between thermal diffusion temperature and material hardness improvement effect, with 970 ℃ as the optimal heat treatment temperature under these experimental conditions.

3.1.2 XRD Analysis of 12Cr2Ni4A Steel After Thermal Diffusion

The X-ray diffractometer analysis was demonstrated in Fig. 8. The diffraction peaks of four phases (Fe, Cr, Ni, and C) were illustrated in Fig. 8. The diffraction peak intensities of Fe, Cr, and Ni phases manifest relatively stable features. The diffraction peaks of Fe-C/Cr-C/Ni-C carbide phases indicated pronounced differences as a function of material type and heat treatment temperature.

The Fe-C/Cr-C/Ni-C carbide phases diffraction peak intensity is most prominent following 970 ℃ treatment, and notably weaker after 950 ℃ treatment. The diffraction peak intensity of carbide phases decreased when the treatment temperature exceeded 970 ℃. Material hardness is enhanced with the increase of thermally diffused C content.

3.2 Wear Mass Loss and Wear Morphology Analysis

The wear mass loss was shown in Fig. 9. The wear resistance of the 12Cr2Ni4A steel pin specimens was significantly improved. Under different treatment conditions, the wear loss of the specimens exhibited a declining trend. The specimen treated with nano-diamond at 970 °C demonstrated the most excellent anti-wear performance, with a wear loss of 0.086 g. The wear mass loss reduced 59.81% compared to the untreated specimen. The specimen subjected to thermal diffusion treatment at 990 °C reduced 12.62% compared to the untreated specimen. The wear losses of specimens treated at 960 °C and 980 °C decreased to 0.136 g and 0.107 g, reduced 35.98% and 50.00%, respectively.

The friction coefficient curve was shown in Fig. 10. Specimens subjected to nano-diamond thermal diffusion treatment manifest pronounced regular variations in friction characteristics. During the running-in stage, the friction coefficient exhibits notable fluctuations. As the test progresses, it advances into a stable stage, with the fric-

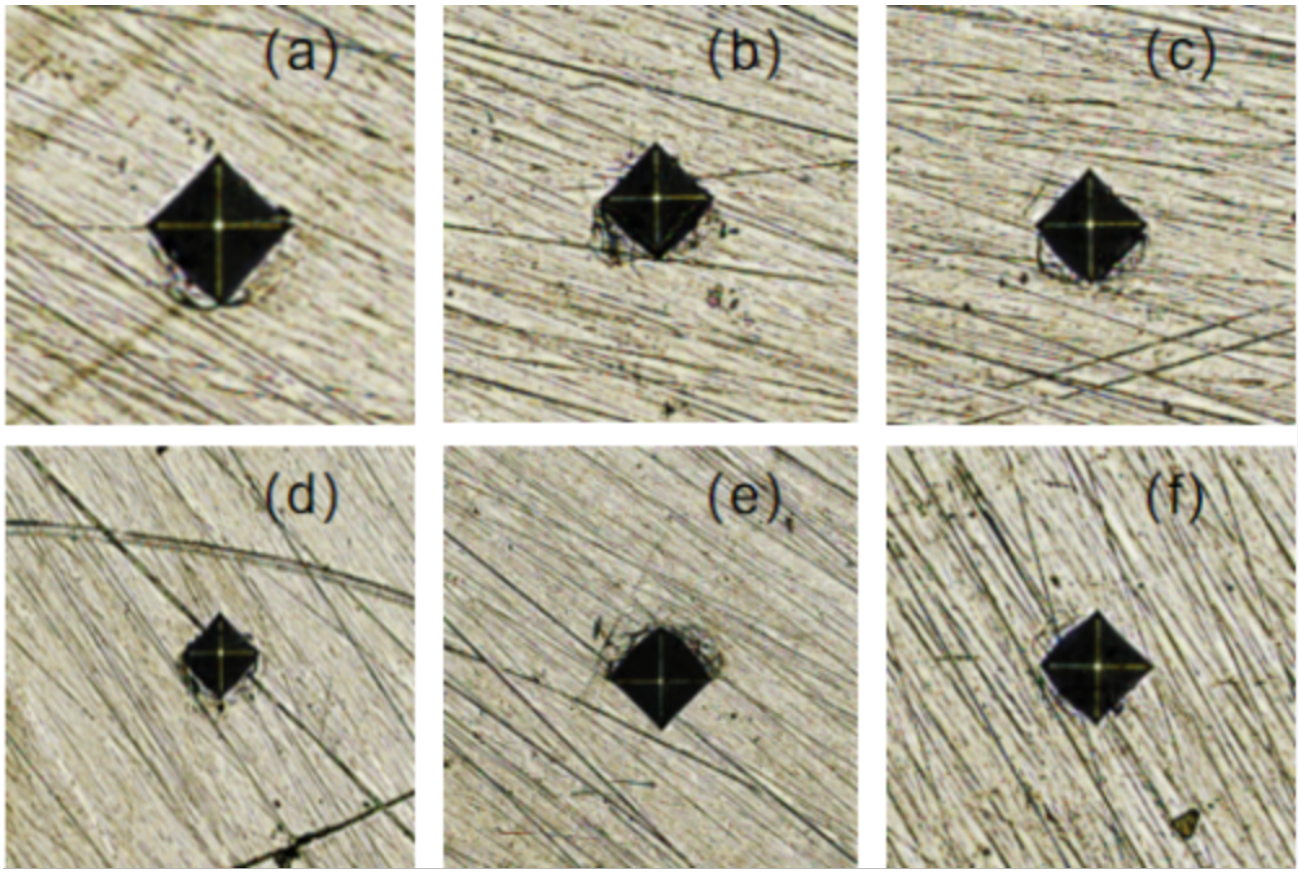

Fig. 7. Hardness indenter morphology image. (a) Primary sample, (b) 950 ℃, (c) 960 ℃, (d) 970 ℃, (e) 980 ℃, (f) 990 ℃.

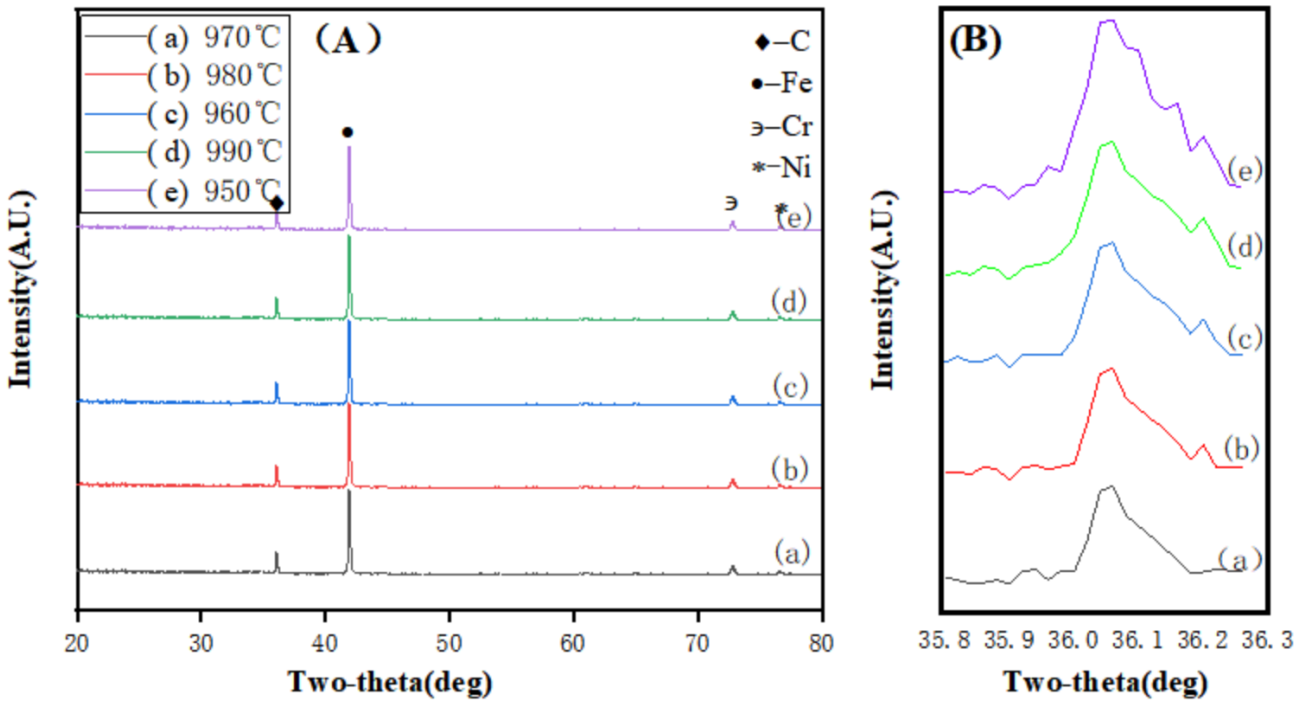

Fig. 8. XRD results of the sample surface after 4 h nano-diamond thermal diffusion. (A) Full-range XRD patterns. (B) Partially enlarged XRD patterns of carbide characteristic peaks. XRD, X-ray diffraction.

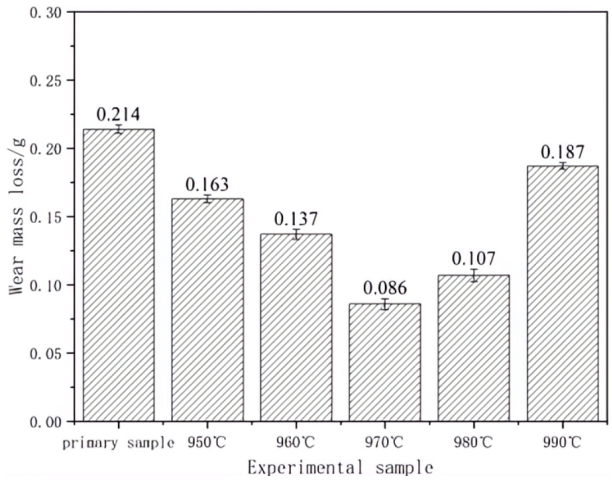

Fig. 9. Wear mass loss of experimental pin after thermal diffusion friction.

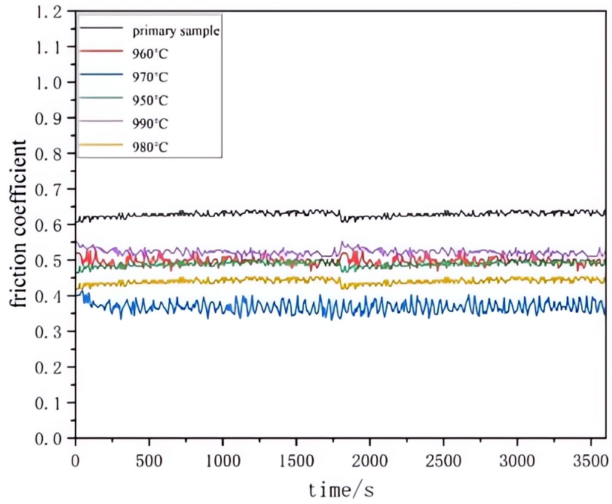

Fig. 10. Friction coefficient curves of tribology test.

tion coefficient stabilizing within a defined range. In the later stage of the experiment, the friction coefficient demonstrates a gradual upward trend.

The average friction coefficient was demonstrated in Fig. 11. The average friction coefficient of the untreated specimen was 0.6285. The wear resistance of 12Cr2Ni4A gear steel pin specimens was significantly enhanced with nano-diamond thermal diffusion treatment.

The 970 ℃ treated specimen exhibited the most pronounced reduction, with its average friction coefficient decreasing to 0.3686 (41.35% reduction compared to the untreated specimen). The friction coefficients of specimens treated at 960 ℃, 980 ℃ and 990 ℃ declined to 0.4974, 0.4408 and 0.5228, corresponding to reductions of 20.86%, 29.86% and 16.83% respectively.

The wear scar areas of 12Cr2Ni3A steel disk specimens in each group were characterized using a super-depth-of-field microscope, as illustrated in Fig. 12.

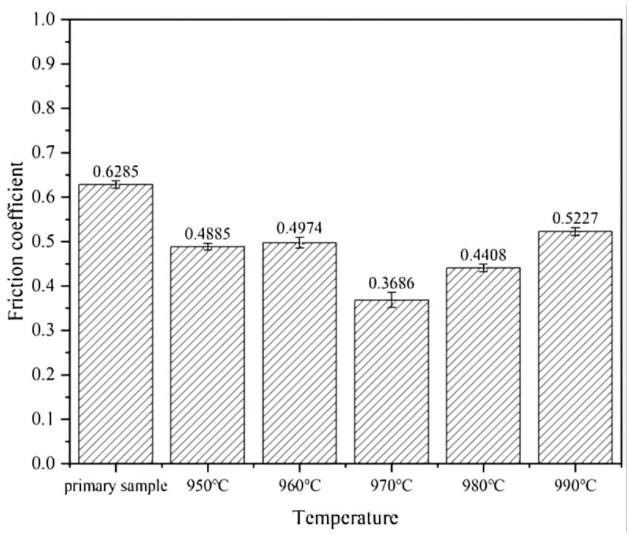

Fig. 11. Average friction coefficient of nano-diamond samples after thermal diffusion friction and wear experiment.

The untreated specimen exhibited a surface groove depth of 0.2 μm, while the specimen treated at 970 ℃ had a groove depth of 8.27 μm in the wear area. The groove depth exhibited a trend of initial increase followed by subsequent decrease as the thermal diffusion treatment temperature rose. The wear scar areas of all nano-diamond treated specimens display grooves of varying depths.

3.3 Molecular Dynamics Simulation Analysis

3.3.1 Analysis of Diffusion Zone

The numerical simulation results of thermal diffusion phenomena based on the molecular dynamics method is shown in Fig. 13. During the initial simulation stage (0 ps, Fig. 13a), all atoms in the system exhibit thermal vibrations around their lattice equilibrium positions, with inter-atomic relative positions maintaining stability.

Following the application of an external thermal field, the system progressively deviates from equilibrium, with atoms migrating from their lattice sites to adjacent regions. This migration behavior intensifies progressively with prolonged thermal field application, and a distinct atomic diffusion zone is finally formed at the interface.

According to literature reports, a diffusion region was considered to be formed when the number of diffusing atoms exceeds 5% [29]. This study systematically analyzed five different time stages (20, 40, 60, 80, and 100 ps) under thermal field action. Through slice calculations, the atomic number ratio distribution at the interface between nano-diamond and Fe, Cr, Ni crystals was obtained (Fig. 14). The thicknesses of the diffusion zones at each stage were 2.3, 3.9, 5.1, 6.0, and 6.8 nm, respectively. The thickness of the diffusion zone exhibits a clear increasing trend with time: when the simulation time extended from 20 ps to 100 ps, the thickness increased from 2.3 nm to 6.8 nm, representing an increase of 2.96 times.

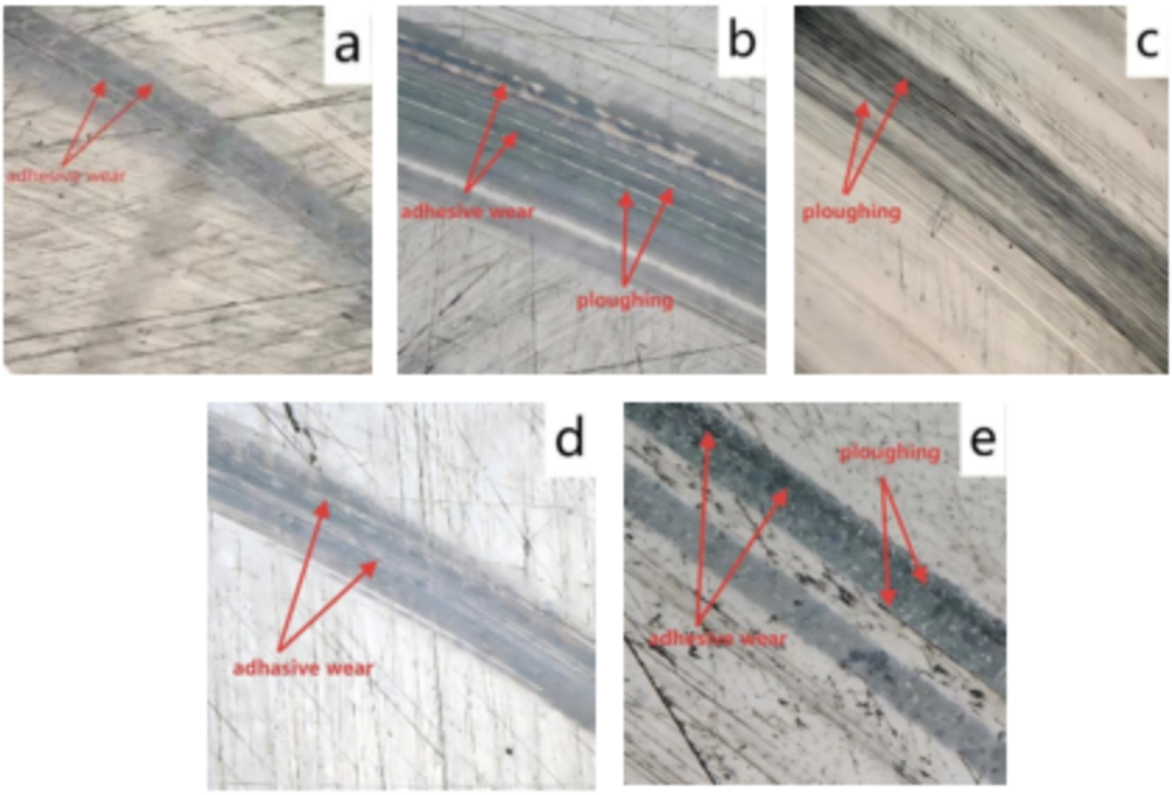

Fig. 12. Wear trace morphology of experimental disc. (a) 950 ℃, (b) 960 ℃, (c) 970 ℃, (d) 980 ℃, (e) 990 ℃.

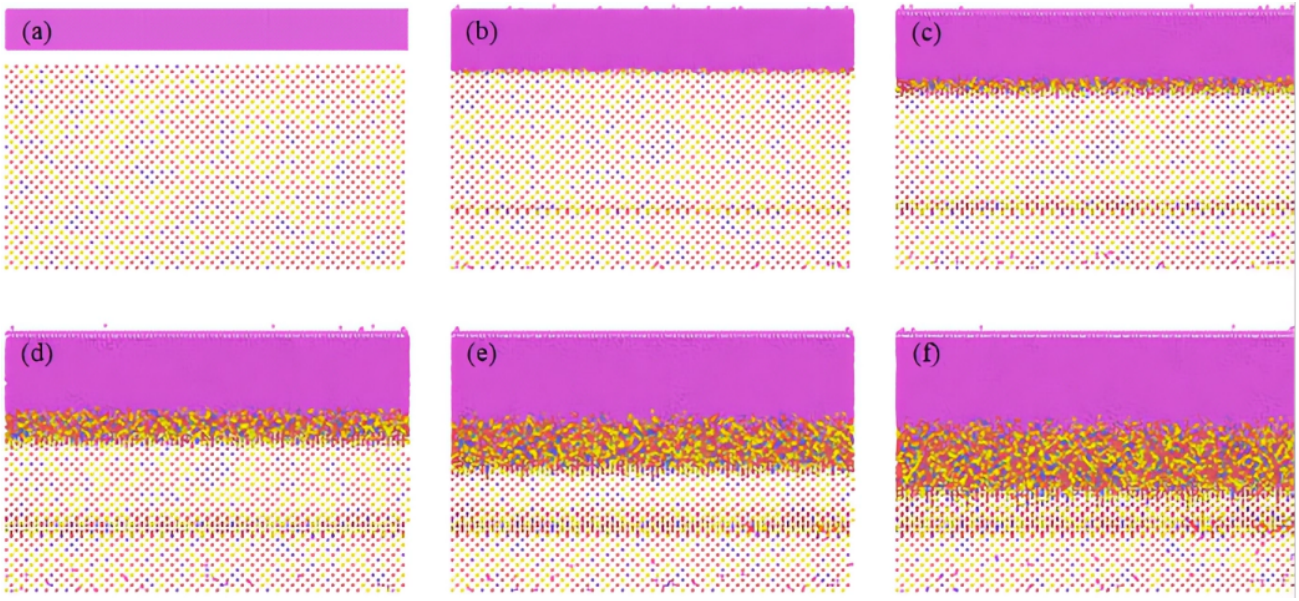

Fig. 13. Molecular dynamics atomic diffusion at different incubation times. (a) 0 ps, (b) 20 ps, (c) 40 ps, (d) Constant temperature 60 ps, (e) Constant temperature 80 ps, (f) Constant temperature 100 ps.

3.3.2 Diffusion Displacement Analysis

Fig. 15 illustrates the displacement distribution characteristics of C-Fe atomic pairs at different constant temperature stages (0, 20, 40, 60, 80, and 100 ps). At the initial moment (0 ps), all atoms are confined to thermal vibrations near their lattice equilibrium positions, showing no obvious migration characteristics. When the system reaches 40 ps, displacement vectors of C-Fe, C-Cr, and C-Ni atomic pairs begin to appear in the interfacial region between nanodiamond and transition metals (Fe, Cr, Ni), marking the preliminary formation of interfacial diffusion behavior.

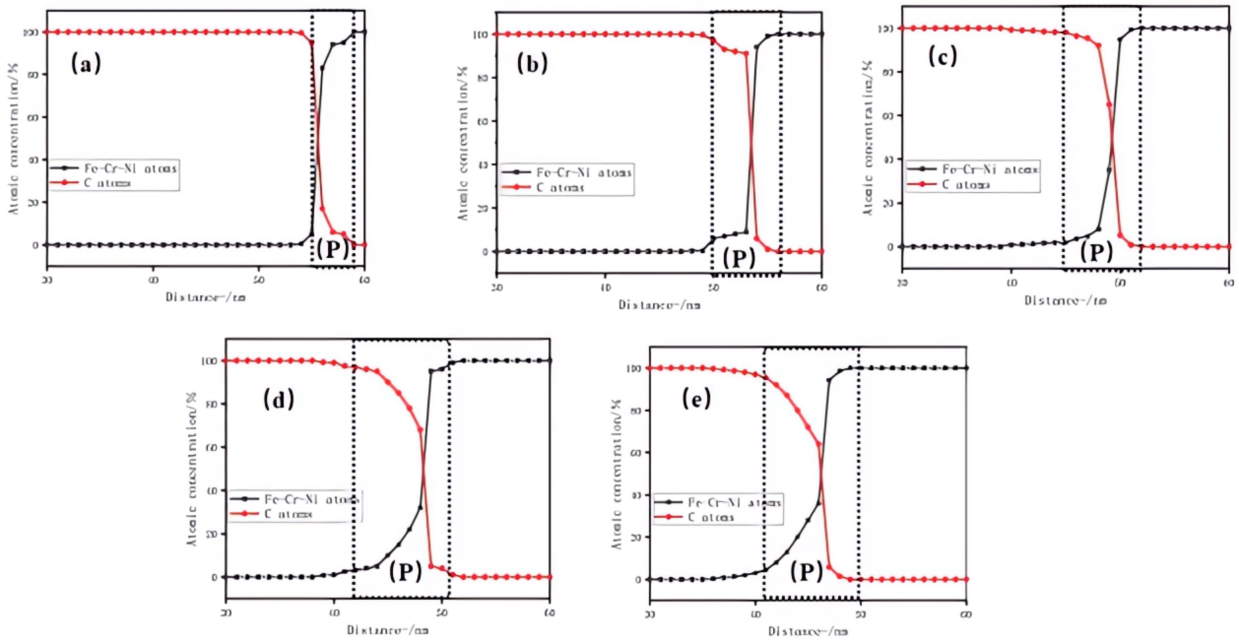

Fig. 14. Variation of atomic quantity ratio at the interface. (a) Constant temperature 20 ps, (b) Constant temperature 40 ps, (c) Constant temperature 60 ps, (d) Constant temperature 80 ps, (e) Constant temperature 100 ps.

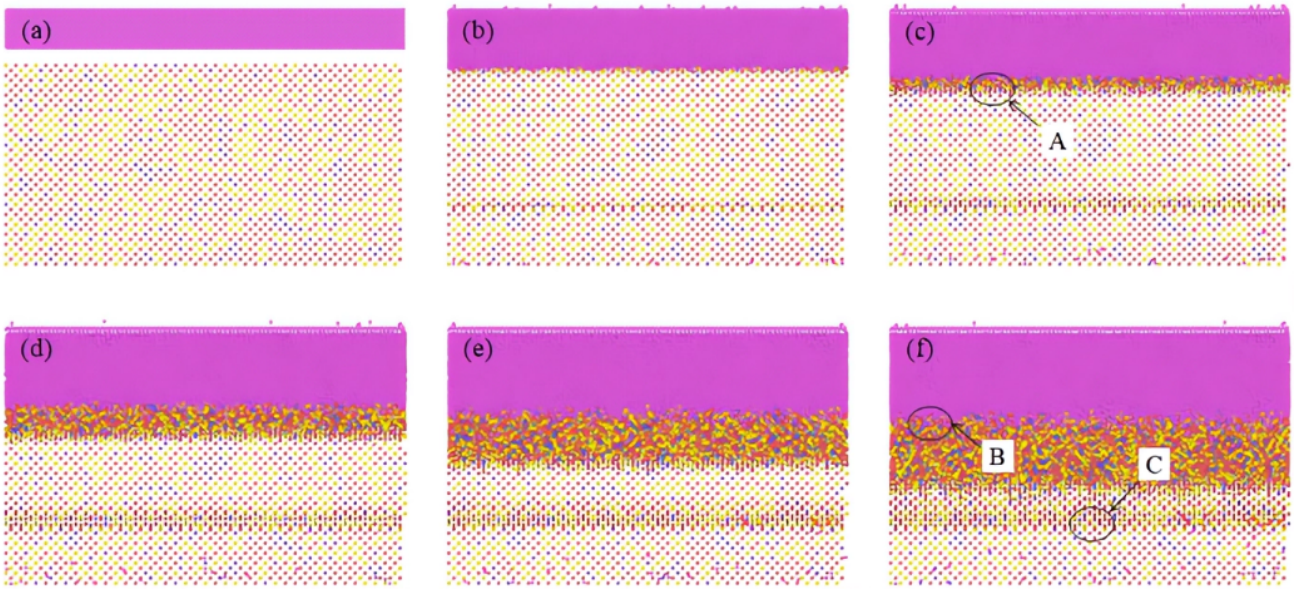

Fig. 15. Atomic displacement vector diagram. (a) Initial state energy minimization 0 ps, (b) Constant temperature 20 ps, (c) Constant temperature 40 ps, (d) Constant temperature 60 ps, (e) constant temperature 80 ps, (f) Constant temperature 100 ps. Labels A, B, and C indicate the local characteristic regions discussed in the main text.

With the extension of simulation time, the number of displacements of C-Fe, C-Cr, and C-Ni atomic pairs in the interfacial region shows a clear increasing trend (Fig. 15c–f). Localized magnification analysis on the atomic displacement vectors (Fig. 16) shows that, due to the smaller covalent radius of C atoms, C atoms can achieve long-range diffusion through lattice interstitial sites, and both the number and distance of C atom migrations significantly exceed those of Fe, Cr, Ni transition metal atoms [30].

3.3.3 Interface Reaction Analysis

Fig. 17 systematically depicts the bonding evolution process between Fe, Cr, Ni atoms and C atoms during diffusion. As illustrated in Fig. 17b, at the 40 ps isothermal stage, free C atoms gradually approach transition metals (Fe, Cr, Ni) and initiate the formation of a small number of Fe-C, Cr-C, and Ni-C bonds—this phenomenon is marked by arrow D in Fig. 17. With extended simulation time, within the 60–100 ps interval (Fig. 17d,e), the number of transition

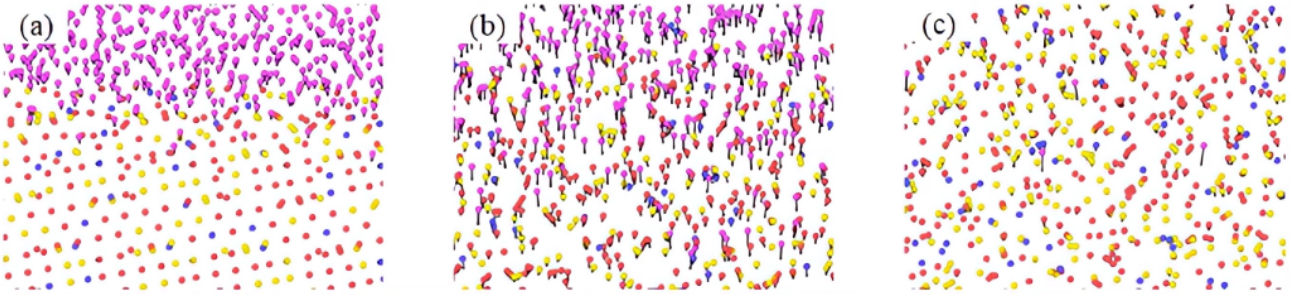

Fig. 16. Partial enlarged views of the atomic displacement vector. (a) Region A; (b) Region B; (c) Region C.

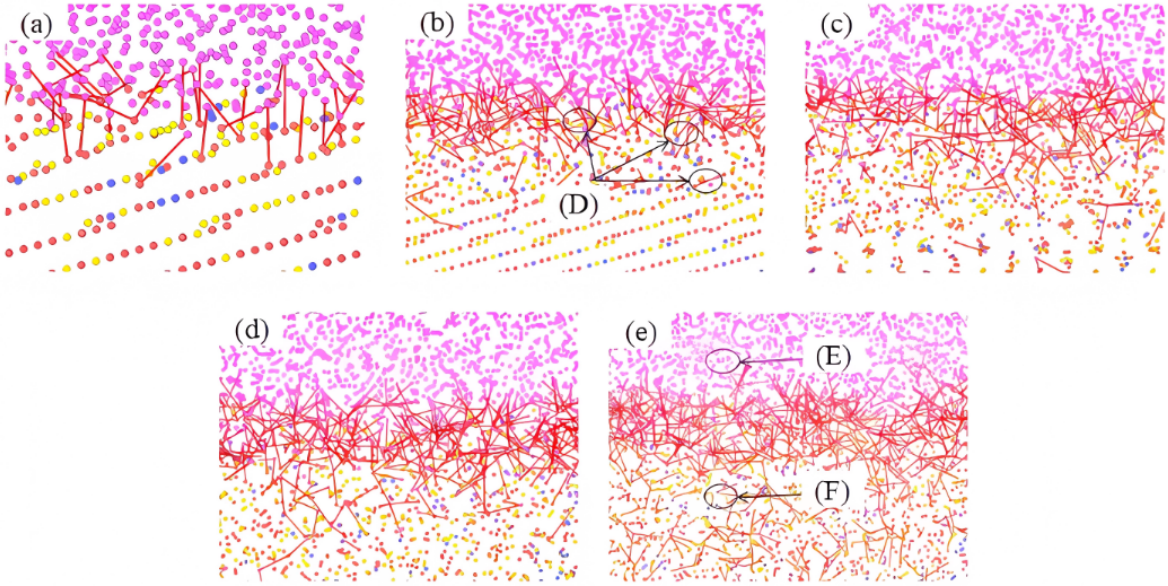

Fig. 17. Fe-C, Cr-C, and Ni-C bonding during atomic diffusion. (a) Initial state energy minimization 20 ps, (b) Constant temperature 40 ps, (c) Constant temperature 60 ps, (d) Constant temperature 80 ps, (e) Constant temperature 100 ps. Labels D, E, and F indicate the local characteristic regions discussed in the main text.

metal-C bonds in the interfacial region exhibits a significant upward trend, ultimately leading to the formation of abundant Fe-C, Cr-C, and Ni-C bonds between nano-diamonds and FeCrNi crystals.

Fig. 17 clearly illustrates the dynamic evolution of nano-diamond diffusion behavior in the metal matrix with prolonged holding time. During the initial holding stage (20 ps, Fig. 17a), driven by the thermal field, some nano-diamond particles acquire sufficient kinetic energy to diffuse into the metal crystal interior while retaining their complete crystal structure. By 40 ps (Fig. 17b), enhanced thermal activation induces structural decomposition of partial nano-diamond particles, transforming them from intact crystal structures into free C atom states.

At the extended holding time of 100 ps (Fig. 17e), the system manifests distinct regional diffusion characteristics: in the upper diffusion zone, the vast majority of nano-diamond particles preserve their original crystal structure; in the lower metal matrix region of the diffusion zone, nano-diamonds primarily exist as free C atoms and continue diffusing. This spatial distribution difference is clearly distinguishable via regions E and F marked in Fig. 17, where region E represents the aggregation area of undecomposed nano-diamond particles, and region F denotes the diffusion front of free C atoms in the metal matrix [28,31,32].

4. Discussion

4.1 Strengthening Mechanism of Nano-Diamond Thermal Diffusion on 12Cr2Ni4A Steel

The non-linear relationship between thermal diffusion temperature and surface hardness of 12Cr2Ni4A steel, is essentially the result of the competition between thermal activation-induced strengthening and high-temperature-induced microstructure deterioration.

At 950–970 °C, the rising temperature provides sufficient activation energy for carbon atoms from nano-diamonds. On one hand, active carbon atoms diffuse into the interstitial sites of Fe-Cr-Ni matrix lattice, causing lattice distortion and realizing interstitial solid solution strengthening, which improves the deformation resistance

of the matrix. On the other hand, diffused carbon atoms combine with Fe, Cr, Ni elements to form nano-scale dispersed Fe-C/Cr-C/Ni-C carbides, which act as strong obstacles to dislocation movement during plastic deformation, bringing a significant dispersion strengthening effect. The peak carbide diffraction intensity at 970 ℃ corresponds exactly to the maximum hardness value, which directly proves that carbide formation is the core source of hardness improvement.

When the temperature exceeds 970 ℃, the strengthening effect weakens sharply. This is mainly attributed to two factors: first, excessively high temperature leads to austenite grain coarsening of 12Cr2Ni4A steel, which reduces the grain boundary strengthening effect after cooling; second, Ostwald ripening of carbide phases occurs under high temperature, the fine dispersed carbides merge and grow up, which greatly weakens the dispersion strengthening effect. The combined effect of the two leads to the only 26.09% hardness improvement at 990 ℃.

4.2 Tribological Performance Enhancement Mechanism of Modified Steel

The significant improvement of wear resistance and friction reduction performance of the modified 12Cr2Ni4A steel, is the synergistic result of hardness enhancement, self-lubrication effect and tribochemical film formation.

In line with Archard's wear law, the wear rate of material is inversely proportional to its hardness under the same wear conditions. The 110.68% hardness increase of the 970 ℃ treated sample directly enhances the material's resistance to plastic deformation and micro-cutting during friction, which is the core reason for the 59.81% wear mass loss reduction and 41.35% friction coefficient reduction. The change of wear scar groove depth also reflects the transition of wear mechanism: the main wear mechanism shifts from severe adhesive wear for the untreated sample to mild abrasive wear for the modified sample, which further confirms the improvement of wear resistance.

In addition, the dual existence form of carbon elements in the modified layer also plays a key role in friction reduction. During friction, intact nano-diamond particles act as nano-scale ball bearings between friction pairs, reducing the shear stress of the contact surface; meanwhile, under the action of friction heat and shear force, free carbon atoms form a graphitized carbon-based lubricating film on the friction surface, which effectively isolates the direct contact between metal matrixes, reduces the fluctuation of friction coefficient in the running-in stage, and prolongs the stable friction stage. For the 990 ℃ treated sample, the limited hardness improvement and coarse grain structure lead to the deterioration of surface load-bearing capacity, the lubricating film is easy to break during friction, so the anti-wear and friction reduction performance is significantly weakened.

4.3 Atomic-Scale Interpretation of Thermal Diffusion Behavior via Molecular Dynamics Simulation

The molecular dynamics simulation results provide direct atomic-scale evidence for macroscopic experimental phenomena, and reveal the thermal diffusion kinetic mechanism of nano-diamond in 12Cr2Ni4A steel matrix.

Under thermal activation, carbon atoms from nano-diamonds diffuse into the Fe-Cr-Ni matrix through interstitial sites, which is consistent with the classical interstitial diffusion mechanism. The diffusion zone thickness increases significantly with prolonged thermal action time, which directly explains the enhanced strengthening effect with rising temperature at 950–970 ℃: higher temperature and longer holding time promote more sufficient carbon diffusion, thus bringing a more significant strengthening effect.

Meanwhile, the simulation reveals the dual existence form of nano-diamond during diffusion: intact particles in the near-interface region for dispersion strengthening, and decomposed free carbon atoms in the deep matrix for solid solution and carbide precipitation strengthening. The Fe-C/Cr-C/Ni-C bonding evolution observed in the simulation is exactly the microscopic origin of the carbide diffraction peaks detected by XRD, which builds a complete bridge between atomic-scale diffusion behavior and macroscopic mechanical properties of the material.

4.4 Advantages of the Proposed Method and Research Prospects

Compared with conventional surface modification technologies for 12Cr2Ni4A steel, the nano-diamond thermal diffusion technology proposed in this study has significant core advantages. Existing technologies such as vacuum carburization combined with Ti+N ion implantation can only improve nano-hardness by ~35% with a strengthened layer thickness of only ~200 nm [5], and rare earth-assisted carburization usually achieves a hardness improvement of 40–50% [6]. In contrast, the proposed technology achieves a 110.68% hardness increase and 59.81% wear mass loss reduction, and can form a micron-scale thick strengthened layer, which can meet the long-term service requirements of heavy-duty gear components under harsh working conditions. Meanwhile, this process has the characteristics of simple operation, low equipment requirement and strong applicability, with broad industrial application prospects.

4.5 Limitations

The molecular dynamics model employed in this study involves simplifications of the actual microstructure of 12Cr2Ni4A steel. The multicomponent alloy is reduced to an idealized Fe-Cr-Ni crystal model, without considering complex defects such as grain boundaries. The Lennard-Jones potential is used to describe the non-bonded interactions between metal and carbon atoms, which is suitable

for capturing atomic diffusion trends but cannot accurately describe the formation and breaking of chemical bonds. These simplifications are intended to focus on revealing the core qualitative mechanisms of carbonatom diffusion and interfacial interactions. The consistency between the model's predictions and the macroscopic performance improvements validates its effectiveness within the research framework.

This study confirms the strengthening effect of nano-diamond thermal diffusion on 12Cr2Ni4A steel, yet certain limitations remain, such as the lack of surface engineering treatment on the nano-diamonds to optimize their interfacial compatibility. Future research could expand into the validation of diverse high-end application scenarios, for instance, evaluating the performance of this modified material under extreme operating conditions in fields such as aerospace and biomedical applications.

The tribological conclusions of this study are derived from a single, standardized set of operating conditions, which, to some extent, limits the universality of the findings. All experiments were conducted with Mobil 600 XP 100 oil, at room temperature, 50 N load and 300 r/min rotational speed. The performance of the modified layer under more complex conditions was not investigated. Future research can systematically test the tribological performance of the modified layer under the coupled influence of multiple factors, including lubrication, load, and speed.

5. Conclusion

This study employs nano-diamond and 12Cr2Ni4A steel as experimental subjects to explore the influence mechanism of nano-diamond thermal diffusion treatment on the hardness and tribological properties of 12Cr2Ni4A gear steel under varying thermal diffusion temperature conditions. The primary conclusions are as follows:

(1) Nano-diamond thermal diffusion technology substantially enhances the microhardness and tribological properties of 12Cr2Ni4A gear steel. Specimen hardness rises from an initial 220.0 HV to 463.5 HV, which increases 110.68%. Wear mass loss is reduced by 59.81%, and the friction coefficient decreases by 41.35%.

(2) Molecular dynamics simulation results indicate that Fe-C, Cr-C, and Ni-C chemical bonds form at the diffusion interface. The surface layer is primarily characterized by a complete diamond structure; with increasing diffusion depth, carbon atoms enter Fe, Cr, and Ni lattices in a free state. This elevation in C content within the 12Cr2Ni4A steel matrix substantially enhances the compactness and bonding strength of the diffusion layer, consequently resulting in significant improvement of its tribological properties.

Availability of Data and Materials

The datasets used and analyzed during the current study are available from the corresponding author on reasonable request.

Author Contributions

LW, SC and XZ designed the study; YL, CL and PX performed the experimental work; YC and HW analyzed the experimental data. MX conducted the data processing and analysis. All authors critically revised the core academic content of the work. All authors read and approved the final manuscript. All authors have participated sufficiently in the work and agreed to be accountable for all aspects of the work.

Ethics Approval and Consent to Participate

Not applicable.

Acknowledgment

Not applicable.

Funding

This project was supported by the National Natural Science Foundation of China (Grant No. 52475056&52575059), the Hunan Provincial Department of Education Fund (Grant No. 24A0462), Open Fund of State Key Laboratory of Special Materials Surface Protection (Grant No. CBQZJJ2024-2-03), Aid Program for Science and Technology Innovative Research Team in Higher Educational Institutions of Hunan Province (High Performance Manufacturing Processes and Service Performance Optimisation).

Conflict of Interest

The authors declare no conflict of interest. Lei Wei is affiliated with the State Key Laboratory of Special Materials Surface Protection, China Academy of Machinery Wuhan Research Institute of Materials Protection Co., Ltd.. China Academy of Machinery Wuhan Research Institute of Materials Protection Co., Ltd. was not involved in the preparation or publication of the manuscript. There is no potential conflict of interest arising from China Academy of Machinery Wuhan Research Institute of Materials Protection Co., Ltd.

References

[1] Kaiser D, Damon J, Mühl F, De Graaff B, Kiefer D, Dietrich S, *et al*. Experimental investigation and finite-element modeling of the short-time induction quench-and-temper process of AISI 4140. Journal of Materials Processing Technology. 2020; 279: 116485. https://doi.org/10.1016/j.jmatprotec.2019.116485.

[2] Karthikeyan KM, Balasubramanian T, Thillaivanan V, Jangetti GV. Laser transformation hardening of EN24 alloy steel. Materials Today: Proceedings. 2020; 22: 3048–3055. https://doi.org/10.1016/j.matpr.2020.03.440.

[3] Aprilia A, Maharjan N, Zhou W. Decarburization in Laser Surface Hardening of AISI 420 Martensitic Stainless Steel. Materials (Basel, Switzerland). 2023; 16: 939. https://doi.org/10.3390/ma16030939.

[4] Liu H, Tang J, Liu C, Liu Y, Jiang W, Sun B. Understanding the distinction between quenching and carburizing quenching stress

field: Evolution mechanism of quenching stress field influenced by carbon content in low-carbon alloy steel. Surface and Coatings Technology. 2024; 489: 131112. https://doi.org/10.1016/j.surfcoat.2024.131112.

[5] Dong M, Cui X, Jin G, Wang H, Cai Z, Song S. Improved microstructure and properties of 12Cr2Ni4A alloy steel by vacuum carburization and Ti+ N co-implantation. Applied Surface Science. 2018; 440: 660–668. https://doi.org/10.1016/j.apsusc.2018.01.171.

[6] Dong M, Cui X, Zhang Y, Jin G, Yue C, Zhao X, *et al*. Vacuum carburization of 12Cr2Ni4A low carbon alloy steel with lanthanum and cerium ion implantation. Journal of Rare Earths. 2017; 35: 1164–1170. https://doi.org/10.1016/j.jre.2017.04.004.

[7] Wang C, Zhou LC, He Q, An ZF, Lu JZ. Experiment research on improving the fatigue life of 12Cr2Ni4A welding joints by laser shock processing. Applied Mechanics and Materials. 2010; 43: 467–470. https://doi.org/10.4028/www.scientific.net/AMM.43.467.

[8] Zhao J, Li C, Zhan H, Yu M, Han X. Study on laser quenching of aircraft gears with rectangular beam based on multi-field coupling mechanism. Applied Physics A. 2025; 131: 47. https://doi.org/10.1007/s00339-024-08174-3.

[9] Wen J, Tang J, Zhou W. Study on formation mechanism and regularity of residual stress in ultrasonic vibration grinding of high strength alloy Steel. Journal of Manufacturing Processes, 2021, 66: 608–622. https://doi.org/10.1016/j.jmapro.2021.04.040.

[10] Lei X, Xiang D, Peng P, Niu X, Zhao B, Gao G. Study on surface residual stress of hardened 12Cr2Ni4A alloy steel by ultrasonic vibration-assisted ELID grinding. The International Journal of Advanced Manufacturing Technology. 2022; 118: 641–649. https://doi.org/10.1007/s00170-021-07328-4.

[11] He P, Ding Y, Hu X, Qian L, Wang Y, Li F. Process Research of Surface Laser Phase Transformation Hardening for 42CrMo Material. Photonics. 2024; 11: 1205. https://doi.org/10.3390/photonics11121205.

[12] Dong ZH, Zhang W, Kang HW, Xie YJ, Ebrahimnia M, Peng X. Surface hardening of laser melting deposited 12CrNi2 alloy steel by enhanced plasma carburizing via hollow cathode discharge. Surface and Coatings Technology. 2020; 397: 125976. https://doi.org/10.1016/j.surfcoat.2020.125976.

[13] Mochalin VN, Osswald S, Portet C, Yushin G, Hobson C, Havel M, *et al*. High temperature functionalization and surface modification of nanodiamond powders. MRS Online Proceedings Library (OPL). 2007; 1039: P11-03. https://doi.org/10.1557/PROC-1039-P11-03.

[14] Loganathan A, Rengifo S, Hernandez AF, Zhang C, Agarwal A. Effect of nanodiamond reinforcement and heat-treatment on microstructure, mechanical and tribological properties of cold sprayed aluminum coating. Surface and Coatings Technology. 2021; 412: 127037.

[15] Huang P, Deng W, Qi W, Chen X, Tian J, Wang Y, *et al*. Superlow friction and wear enabled by nanodiamond and hexagonal boron nitride on aC: H films surfaces in dry nitrogen. Materials Today Nano. 2023; 24: 100384. https://doi.org/10.1016/j.mtnano.2023.100384.

[16] Bogatyreva GP, Marinich MA, Zabuga VY, Tsapyuk GG, Panova AN, Bazalii GA. The effect of surface modification on thermal stability of nanodiamonds. Journal of Superhard Materials. 2008; 30: 305–310. https://doi.org/10.3103/S1063457608050043.

[17] Dahale C, Srinivasan SG, Mishra S, Maiti S, Rai B. Surface segregation in the AgAuCuPdPt high entropy alloy: insights from molecular simulations. Molecular Systems Design & Engineering. 2022; 7: 878–888. https://doi.org/10.1039/D2ME00045H.

[18] Zhang G, Luo D, Wu G, Liu D, Wang J, Deng X, *et al*. Effect of carbon nanotubes intensified coolant on the grinding performance of carburizing and quenching 12Cr2Ni4A steel. The International Journal of Advanced Manufacturing Technology. 2023; 124: 3935–3946. https://doi.org/10.1007/s00170-021-08160-6.

[19] Chiganova GA, Mordvinova LE. Effect of nanodiamond modification on the characteristics of diamond-containing nickel coatings. Inorganic materials. 2011; 47: 717–721. https://doi.org/10.1134/S0020168511070089.

[20] Wang D, Li F, Liu M, Zhang W, Yu X, Da W. Effect of Nanodiamond Content in the Plating Solution on the Corrosion Resistance of Nickel–Nanodiamond Composite Coatings Prepared on Annealed 45 Carbon Steel. Coatings. 2022; 12: 1558. https://doi.org/10.3390/coatings12101558.

[21] Sanaka R, Sahu SK. Experimental investigation into mechanical, thermal, and shape memory behavior of thermoresponsive PU/MXene shape memory polymer nanocomposite. Heliyon. 2024; 10: e24014. https://doi.org/10.1016/j.heliyon.2024.e24014.

[22] Zhang B, Liu H, He Y, Guagliano M. The effect of fine particle peening on aviation gear performance, Part I: Surface integrity. Fatigue & Fracture of Engineering Materials & Structures. 2024; 47: 3000–3014. https://doi.org/10.1111/ffe.14355.

[23] Kang H, Zhang Y, Yang M. Molecular dynamics simulation of thermal conductivity of Cu–Ar nanofluid using EAM potential for Cu–Cu interactions. Applied Physics A. 2011; 103: 1001–1008. https://doi.org/10.1007/s00339-011-6379-z.

[24] Nayak P, Naik SR, Sar DK. Improved Cohesive Energy of Metallic Nanoparticles by Using L–J Potential with Structural Effect. Iranian Journal of Science and Technology, Transactions A: Science. 2019; 43: 2705–2711. https://doi.org/10.1007/s40995-019-00752-y.

[25] Yan S, He L. Adhesive force between a spherical rigid particle and an incompressible elastic substrate. Mechanics of Materials. 2012; 49: 66–71. https://doi.org/10.1016/j.mechmat.2011.10.005.

[26] Pestryaev EM. Molecular-dynamics study of chain reptation in a gel. Polymer Science Series A. 2013; 55: 336–352. https://doi.org/10.1134/S0965545X13050052.

[27] Maghfiroh C Y, Arkundato A, Maulina W. Parameters (σ, ε) of Lennard-Jones for Fe, Ni, Pb for potential and Cr based on melting point values using the molecular dynamics method of the Lammps program. Journal of Physics: Conference Series. IOP Publishing. 2020; 1491: 012022. https://doi.org/10.1088/1742-6596/1491/1/012022.

[28] Han B, Cui M, Tong R. Molecular dynamics simulation on friction properties of BCC iron strengthened by nanodiamonds. Molecular Simulation. 2025; 51: 529–545. https://doi.org/10.1080/08927022.2025.2507398.

[29] Yang N, Liu H, Xu F, He Q, Liu X, Mi N. Tribological behavior of high-entropy alloy FeNiCrMn: a molecular dynamics simulation study. RSC Advances. 2025; 15: 34600–34608. https://doi.org/10.1039/d5ra04932f.

[30] Xiong G, Yang C, Zhu W. Interface reaction processes and reactive properties of Al/CuO nanothermite: An ab initio molecular dynamics simulation. Applied Surface Science. 2018; 459: 835–844. https://doi.org/10.1016/j.apsusc.2018.08.069.

[31] Wang H, Han EH. Ab initio molecular dynamics simulation on interfacial reaction behavior of Fe-Cr-Ni stainless steel in high temperature water. Computational Materials Science. 2018; 149: 143–152. https://doi.org/10.1016/j.commatsci.2018.03.025.

[32] Shi A, Zheng H, Chen Z, Zhang W, Zhou X, Rossi C, *et al*. Exploring the Interfacial Reaction of Nano Al/CuO Energetic Films through Thermal Analysis and Ab Initio Molecular Dynamics Simulation. Molecules (Basel, Switzerland). 2022; 27: 3586. https://doi.org/10.3390/molecules27113586.